International Journal of Progressive Sciences and Technologies (IJPSAT)
ISSN: 2509-0119.
© 2026 Scholar AI LLC.
https://ijpsat.org/
Vol. 60 No. 1 November 2026, pp. 496-517

Parametric Analysis And Thermal Modeling Of A Solar Chimney Power Plant For Essential Oil Extraction: Case Study Of Mahajanga, Madagascar

RAHARIJAONA Petera[1], DONA Victorien Bruno[2]

[1]PhD student, Doctoral School of Life Sciences and Modeling (EDGVM), University of Mahajanga, Madagascar
[2]Professor, Laboratory of Applied Physics and Renewable Energies (LPADER), Doctoral School of Life Sciences and Modeling (EDGVM), University of Mahajanga, Madagascar

Corresponding Author: RAHARIJAONA Petera. E-mail: rpetera05@gmail.com, bvdno2@gmail.com

(cc) BY

Abstract: This study evaluates the thermal performance of a solar chimney power plant intended to generate steam for essential oil extraction in Mahajanga, Madagascar. Analysis of meteorological data from 2010 to 2024 characterizes the site's solar potential and identifies January and October as the unfavorable and favorable months, respectively. The methodology combines a seven-node thermal model, transient simulation, and experimental extraction results. Maximum solar irradiances reach 655.57 W.m-2 in January and 949.57 W.m-2 in October. The methodology relies on a seven-node thermal model combined with a parametric analysis of solar irradiance, air mass flow rate, glazing properties, and water depth. Comparison of quasi-steady-state and transient regimes reveals a thermal delay of 2 h 36 min, mainly due to water thermal inertia. The results show that the Glass–Low-E combination and a 1 cm water layer promote heating and vaporization. At 1 bar absolute pressure, theoretical steam production reaches 31.57 kg in October, with a maximum flow rate of 11.10 kg.h-1, compared with zero production in January. Experimental trials on Niaouli, Kininina, and Ravintsara give essential oil yields of 0.13 to 1% and average recovered condensate flow rates of 1.08 to 8.82 kg.h-1. These findings indicate that the solar chimney power plant can help supply steam to the still during the favorable month, provided that sufficient flow and efficient steam transport to the extraction vessel are ensured.

Keywords: Mahajanga; solar potential; solar chimney power plant; thermal storage; transient regime; water vapor; essential oils.

1. INTRODUCTION

The Mahajanga region is characterized by rich plant biodiversity, including various endemic species of pharmacological, agri-food, and especially economic interest.

To achieve higher yields, several factors must be considered when extracting essential oils in a still, including the type of boiler used, extraction method, plant species, quantity of plant material, and, most importantly, steam temperature [1]. Traditional systems using wood-fired boilers, charcoal, or fuel oil have long been used for extraction by either steam distillation or hydrodistillation [1], [2]. Furthermore, climate change and technological advances have encouraged researchers to develop new systems such as electric boilers using heating elements and solar boilers using solar thermal collectors or concentrators [3], [4], [5].

A solar chimney power plant (SCPP) operates by heating air beneath a solar collector and driving its upward flow through a chimney by thermal buoyancy. Primarily developed for electricity generation, it has been the subject of numerous theoretical and

experimental studies on its energy performance and the influence of its geometric and thermal parameters [6], [7], [8], [9], [10]. The integration of water-based thermal storage has also been investigated to modify the collector's thermal behavior and extend energy availability [11], [6].

Bernardes et al. [10] notably demonstrated the importance of the collector's geometric and optical characteristics for solar chimney power plant performance. In a complementary approach, Semai [6], [12] studied the thermal modeling of an SCPP incorporating water storage, while Achouri [13] experimentally investigated the thermal behavior of a solar chimney device coupled with a storage system. These studies provide a basis for analyzing heat transfer within the collector. However, temperatures calculated using a steady-state model alone cannot establish the time required to heat the water or demonstrate actual steam generation.

Against this background, the present study proposes coupling a solar chimney power plant with a still for essential oil extraction. The system comprises a solar collector, a water basin serving as a solar boiler, and a chimney that promotes airflow. The basin is covered with low-emissivity glazing to limit heat losses. The generated steam is intended to be conveyed to the extraction vessel. The study also draws on experimental results obtained at the Essential Oil Extraction Unit of the Faculty of Science, Technology and Environment, University of Mahajanga, equipped with a 500-liter semi-industrial still and a 250-liter boiler.

The objective of this work is to evaluate the plant's thermal performance and steam-generation potential under the climatic conditions of Mahajanga. The methodology uses meteorological data from 2010 to 2024 and a seven-node thermal model. A parametric analysis examines the effects of solar irradiance, air mass flow rate, glazing properties, and water-layer thickness. Comparing quasi-steady-state and transient regimes makes it possible to assess thermal inertia, while including phase change enables estimation of steam production. Finally, numerical results are compared with experimental extraction data for niaouli, kininina, and ravintsara to assess the coupling potential between the solar plant and the still.

2. MATERIALS AND METHODS

2.1. Description and configuration of the system studied

An experimental essential oil extraction unit was installed at the Faculty of Science, Technology and Environment (FSTE), Ambondrona campus, University of Mahajanga. It includes a stainless-steel extraction vessel with a capacity of 500 L, a diameter of 1.28 m, and a height of 1.65 m. The system is equipped with a conventional 250 L boiler, 0.80 m in diameter and 1.00 m high, and a condenser 0.58 m in diameter and 0.88 m high. The assembly is housed under a 4 m × 6 m shelter (Figure 1).

This installation was used to carry out extraction trials on various aromatic plants, notably kininina, niaouli, and ravintsara. The volumes of essential oil collected, masses of plant material treated, and extraction times constitute the experimental data used to characterize the conventional process.

International Journal of Progressive Sciences and Technologies (IJPSAT)
ISSN: 2509-0119.
© 2026 Scholar AI LLC.
https://ijpsat.org/
Vol. 60 No. 1 November 2026, pp. 496-517

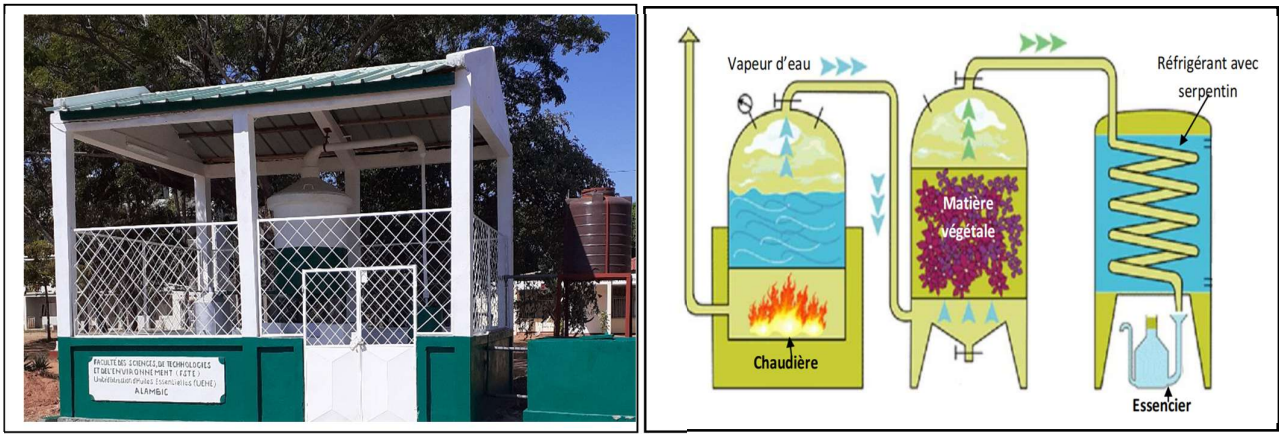

Figure 1: Experimental essential oil extraction installation at FSTE Mahajanga and its operating principle

In principle, the water-filled absorber basin serves both as a storage system for the solar chimney power plant and as a boiler producing steam for the still. Water in the boiler basin is heated by the SCPP solar collector through the greenhouse effect until it reaches boiling temperature. The steam produced is then conveyed to the still containing the plant material to be extracted. Under the action of pressure and temperature, the essential oil is released with the water vapor, which is condensed in the condenser so that floral water and essential oil can be separated in the oil separator. The proposed solar chimney still consists of a single-glazed solar chimney tower; an absorber basin fitted with a low-emissivity glass cover; a still vessel containing green plant material; and a condenser.

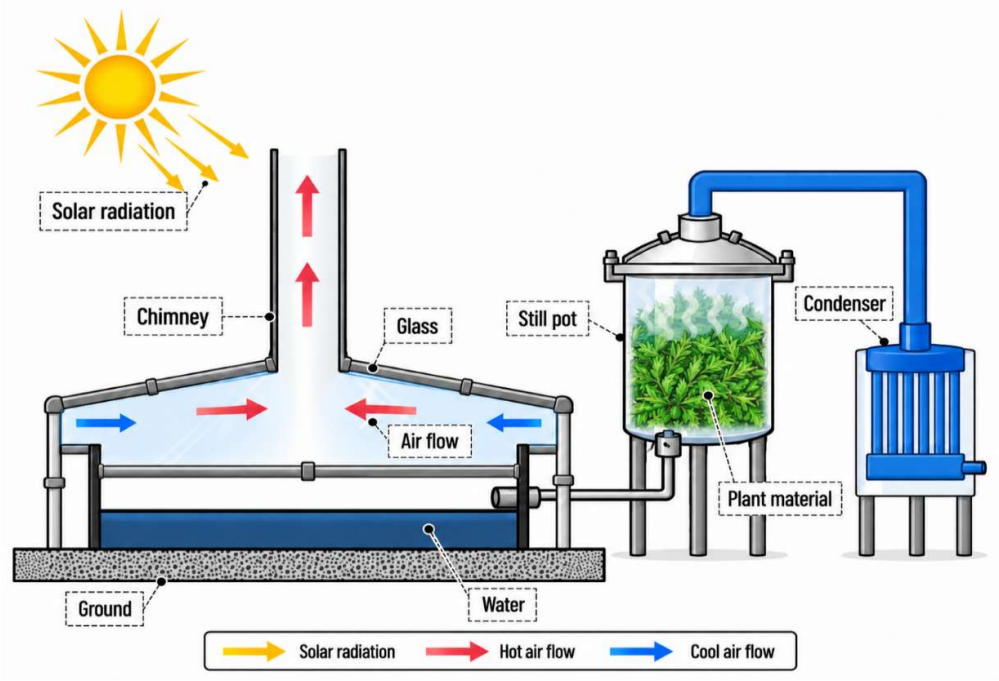

Figure 2: Thermal coupling between the solar chimney power plant and the essential oil extraction still

International Journal of Progressive Sciences and Technologies (IJPSAT)
ISSN: 2509-0119.
© 2026 Scholar AI LLC.
https://ijpsat.org/
Vol. 60 No. 1 November 2026, pp. 496-517

To identify a configuration suitable for the intended application, five cases inspired by previous prototypes and studies were considered. Their geometric characteristics and thermal performance were compared to identify a configuration appropriate for the proposed device's scale. This comparison provides the reference configuration used for the steady-state parametric study. The most favorable thermal conditions are then subjected to transient analysis to examine how water inertia affects heating and the possible attainment of saturation temperature.

- First case: Manzanares prototype [12]. This installation comprises a chimney 194.6 m high and 10.16 m in diameter, and a collector 244 m in diameter. At a solar irradiance of 600 $W \cdot m^{-2}$, the simulation considered in this study yields a water temperature of approximately 60 °C at solar noon.
- Second case: model proposed by Barison James [14]. This configuration comprises a chimney 20 m high and 0.5 m in diameter, coupled with a collector 6 m in diameter. The water depth considered is 10 cm. The water temperature reported in the manuscript is 42 °C.
- Third case: Krisst prototype [15]. This device has a chimney 10 m high and 0.2 m in diameter, with a collector 6 m in diameter positioned 0.5 m above the ground. Under the meteorological conditions considered and an assumed 5 cm water layer, the simulation yields a water temperature of approximately 67 °C.
- Fourth case: Kasdi Merbah University, Ouargla prototype [13]. The experimental device includes a 4 m-high chimney and a 3 m-diameter collector tilted at 5°. A system comprising, in particular, a black tube filled with water and gravel is used for thermal storage. A water temperature of approximately 65 °C is reported under the experimental conditions presented.
- Fifth case: Mansoura University prototype [16]. The device is described in the manuscript as a square collector of approximately 100 m², coupled with a chimney 8 m high and 0.3 m in diameter. Under the meteorological conditions considered, the simulation yields a maximum water temperature of approximately 77 °C.

2.2. Estimation of solar radiation from sunshine-duration data

The evaluation of the solar chimney power plant's thermal performance is based on meteorological conditions at the Mahajanga site. Sunshine-duration records from the ASECNA Mahajanga meteorological station for 2010–2024 are used to estimate solar radiation incident on the collector.

Mean daily global solar irradiation on a horizontal surface is determined using the empirical Ångström–Prescott relationship [17].

$$\begin{cases} \frac{H}{H_0} = a + b \times (\sigma) & (1) \\ \sigma = \frac{S}{S_0} \; ; \; S_o = \frac{2}{15}\omega_s & (2) \\ K_T = \frac{H}{H_0} & (3) \\ H = K_T \times H_0 & (4) \end{cases}$$

Where: $\left\{ H_0 = \frac{24}{\pi} I_{sc.} \left(1 + 0,033.\cos\left(\frac{360N}{365}\right)\right)\left(\cos(\varphi)\cos(\delta)\sin(\omega_s) + \frac{2\pi\omega_s}{360}\sin(\varphi)\sin(\delta)\right)\right.$

The hourly distribution of solar radiation is estimated using the Liu and Jordan relationships [34], taking into account solar position and astronomical day length. Radiation incident on the collector is calculated from its direct, diffuse, and ground-reflected components according to the geometry considered.

International Journal of Progressive Sciences and Technologies (IJPSAT)
ISSN: 2509-0119.
© 2026 Scholar AI LLC.
https://ijpsat.org/
Vol. 60 No. 1 November 2026, pp. 496-517

$$\begin{cases} H_t = H_b R_b + H_d\left(\frac{1+\cos\beta}{2}\right) + H\rho\left(\frac{1-\cos\beta}{2}\right) & (5) \\ I = r_t \times H \\ I_D = I - I_d \\ H_D = H - H_d \\ I_T = I_D \cdot r_{b,T} + I_d\left(\frac{1+\cos\beta}{2}\right) + I.\rho\left(\frac{1-\cos\beta}{2}\right) & (6) \end{cases}$$

2.3. Modeling the thermal performance of the solar chimney power plant

2.3.1. Quasi-steady-state modeling of heat exchange and temperatures in the solar chimney tower

Evaluation of the solar chimney power plant's thermal performance is based on modeling heat exchange among the collector components. The model determines temperature distributions and analyzes the effects of design and operating parameters on the heating of water in the solar basin.

The assumptions adopted in modeling the solar collector are as follows [6], [18]:

-Operating conditions are quasi-steady-state. The sky is treated as a blackbody.

-The collector cover is opaque to infrared radiation. The physical properties of the system components are independent of temperature.

-Flow through the collector is treated as flow between two flat plates.

-There is no evaporation within the collector. Flow through the collector is axisymmetric.

-Heat conduction in the direction of flow is neglected.

-The transverse temperature gradient in the absorber is neglected.

-The ground surface temperature at the absorber interface is assumed equal to the absorber temperature.

The heat-transfer phenomena and equivalent thermal–electrical circuit for the collector are as follows [6].

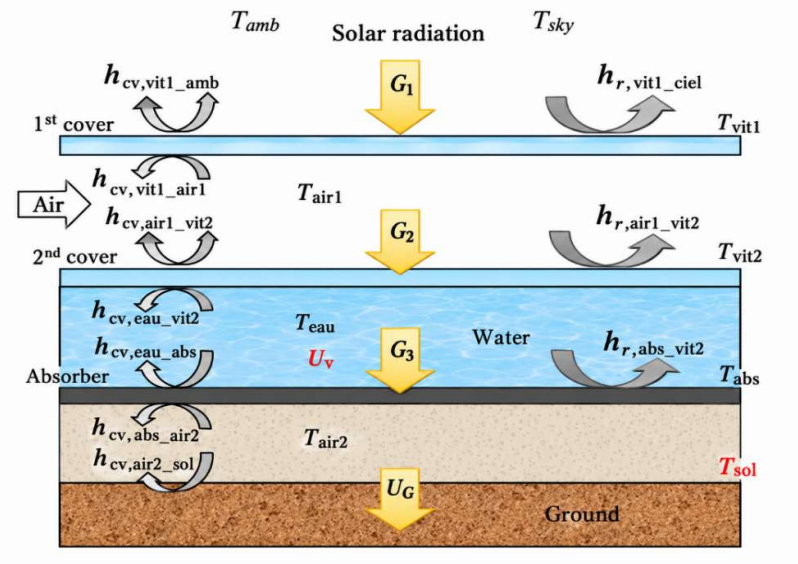

Figure 3: Heat-transfer phenomena within the collector

International Journal of Progressive Sciences and Technologies (IJPSAT)
ISSN: 2509-0119.
© 2026 Scholar AI LLC.
https://ijpsat.org/
Vol. 60 No. 1 November 2026, pp. 496-517

Using the thermal–electrical analogy, each component i of a section Si of the system (still coupled with the SCPP) at time t, having mass Mi, specific heat capacity CPi, and temperature Ti, can be represented by a node at its center, whose temperature equals the component's average temperature. Accordingly, writing the thermal balance (or Ohm's law analogy) for each node yields equations of the following form [6]:

$$M_i C_{Pi} \frac{dT_i}{dt} = \sum_{i=1}^{n} q_i + p_i \qquad (7)$$

Where qi is a source term and pi is a sink term

Applying the nodal balance expressed in Eq. (7) to the various nodes of collector section i yields a system of seven nonlinear, nonautonomous differential equations governing the temperatures of the different collector layers [15]: $T_{vit}, T_{air1}, T_{vit2}, T_{eau}, T_{abs}, T_{air2}$ et T_{sol}

$$\begin{cases} G_1 + h_{r,vit2_vit1}\left(T_{vit2} - T_{vit1}\right) + h_{cv,vit1_air1}\left(T_{air1} - T_{vit1}\right) = h_{cv,vit1_amb}\left(T_{vit1} - T_{amb}\right) + h_{r,vit1_ciel}\left(T_{vit1} - T_{ciel}\right) \\ h_{cv,vit_air1}\left(T_{vit1} - T_{air1}\right) = h_{cv,ver_air1}\left(T_{air1} - T_{vit2}\right) + Q_{u_air} \\ G_2 = h_{cv,eau_vit2}\left(T_{eau} - T_{vit2}\right) + h_{cv,air1_vit2}\left(T_{air1} - T_{vit2}\right) + h_{r,vit1_vit2}\left(T_{vit1} - T_{vit2}\right) + h_{r,vit2_abs}\left(T_{vit2} - T_{abs}\right) \\ h_{cv,vit2_eau}\left(T_{vit2} - T_{eau}\right) = h_{cv,eau_abs}\left(T_{eau} - T_{abs}\right) \\ G_3 = h_{cv,abs_eau}\left(T_{abs} - T_{eau}\right) + h_{cv,abs_air2}\left(T_{abs} - T_{air2}\right) + h_{r,abs_vit2}\left(T_{abs} - T_{vit2}\right) + U_{eau}\left(T_{abs} - T_{amb}\right) \\ h_{cv,abs_air2}\left(T_{abs} - T_{air2}\right) = h_{cv,air2_surfsol}\left(T_{air2} - T_{surf_sol}\right) \\ h_{r,air_surfsol}\left(T_{air2} - T_{surf_sol}\right) = U_{sol}\left(T_{surf_sol} - T_{sol}\right) \end{cases} \qquad (8)$$

Assuming that the temperature varies linearly over each section of the collector, the average temperature can be approximated by the arithmetic mean. The net heat flux transferred to the flowing air may then be expressed as a function of the mean fluid temperature and the inlet air temperature, as follows Assuming a linear temperature distribution across each collector section, the mean temperature is taken as the arithmetic average. The net heat transfer rate to the airflow can therefore be defined in terms of the average fluid temperature and the inlet temperature as follows [6]:

$$Q_{air} = \frac{\dot{m}_{air} C_{p,air}}{\pi r L}\left(T_{air} - T_{air,ent}\right); T_{air} = \frac{T_{air,ent} + T_{air,sort}}{2} \qquad (9)$$

The heat-transfer coefficient in the storage water can be calculated using the following formula [12]:

$$U_{eau} = \frac{1}{t}\sum_{k=0}^{\infty}\left[\frac{2L_{eau}\sin(\delta_k)^2}{\alpha\delta_k\left[\delta_k + \sin(\delta_k)\cos(\delta_k)\right]} e^{\left(-\delta_k^2 \alpha \frac{t_1}{L_{eau}^2}\right)}\right] \qquad (10)$$

The power absorbed by the water layer is given by relation (15) below [19]:

$$Q_{eau} = \dot{m}_e C_{p,e}\left(T_{fs} - T_{fe}\right) + \dot{m}_{vap}.\Delta H_{vap} \qquad (11)$$

The heat-transfer coefficient in the ground is given by the following relation [12]:

$$U_{sol} = 2\sqrt{\frac{k_{sol}\rho_{sol}C_{p,sol}}{\pi t}} \qquad (12)$$

International Journal of Progressive Sciences and Technologies (IJPSAT)
ISSN: 2509-0119.
© 2026 Scholar AI LLC.
https://ijpsat.org/
Vol. 60 No. 1 November 2026, pp. 496-517

2.3.2. Transient modeling of water heating in the solar basin

To examine the effect of water thermal inertia on collector performance, a transient extension of the seven-node steady-state model is considered. The geometric and thermal conditions preselected through parametric analysis are used to compare equilibrium temperatures with those likely to be reached during a sunny day. The model retains the nodal architecture developed by Semai [12] and follows the thermal analysis of solar chimney power plants discussed by Bernardes et al. [10].

Before phase change, conservation of energy in the water basin can be written, assuming uniform water temperature [20]:

$$\dot{Q}_{th,eau}(t) = m_{eau,bac}.c_{p,eau}.\frac{dT_{eau}}{dt} + \dot{m}_{vap}\,\Delta H_{vap} \qquad (13)$$

where m_eau is the water mass, $C_{p,e}$ its specific heat capacity, T_eau its temperature, and $Qth_{,e}$ the instantaneous thermal power stored in the basin.

An expression consistent with the nodal system is [21], [22]:

$$h_{cv,vit2_eau}\left(T_{vit2}^{k+1} - T_{eau}^{k+1}\right) + h_{cv,eau_abs}\left(T_{abs}^{k+1} - T_{eau}^{k+1}\right) = \rho_e e_e\, c_{p,e}\,\frac{T_{eau}^{k+1} - T_{eau}^{k}}{\Delta t} \qquad (14)$$

Heat exchange in the water layer is estimated using a natural-convection correlation based on the Rayleigh and Nusselt numbers. The formulation adopted corresponds to the horizontal arrangement of the correlation proposed by Hollands et al. [23]:

The Rayleigh number is $Ra_e = \frac{g\beta_e \Delta T_e e_e^3}{\nu_e \alpha_e}$ où $\Delta T_e = \max(T_{abs} - T_{pf,0})$ (15)

The Nusselt number used is: $Nu_e = 1 + 1,44\left(1 - \frac{1708}{Ra_e}\right) + \left[\left(\frac{Ra_e}{5830}\right)^{1/3} - 1\right]_+$ (16)

2.3.3. Thermal efficiency of the collector and the chimney

The collector's thermal efficiency can be expressed as the ratio of the heat gained by the air to the solar energy supplied to the collector [24]:

$$\eta_{coll} = \frac{Q_{coll}}{G_{coll}} \quad Avec \quad Q_{coll} = \dot{m} C_p \Delta T_{coll} = \alpha A_{coll} G_H - \beta A_{coll} \Delta T_{coll} \qquad (17)$$

α Effective solar radiation absorption coefficient of the collector.

Energy-loss coefficient accounting for convection, radiation, and ground storage losses. β

The collector's energy efficiency is defined as follows:

$$\eta_{coll} = \alpha - \frac{\beta}{G_H}\Delta T_{coll} \qquad (18)$$

The air mass flow rate at the chimney inlet can be calculated from air density at the collector outlet, the cross-sectional area perpendicular to the chimney axis, and the air velocity at the chimney inlet:

$$\dot{m} = \rho_{coll} \times A_{chem} \times V_{air,chem} \qquad (19)$$

International Journal of Progressive Sciences and Technologies (IJPSAT)
ISSN: 2509-0119.
© 2026 Scholar AI LLC.
https://ijpsat.org/
Vol. 60 No. 1 November 2026, pp. 496-517

Where

$$V_{air,chem} = \frac{\alpha A_{coll} G_H - \beta \Delta T A_{coll}}{\rho_{coll} A_{chem} C_p \Delta T} \quad (20)$$

According to Jörg Schlaich, chimney performance is expressed as follows [16]:

$$\eta_{CHE} = \frac{P_{TOT}}{\dot{Q}} = \frac{g.H_{CHE}}{C_{p,air}.T_{amb}} \quad (21)$$

$$\begin{cases} P_{TOT} = \frac{g H_{CHE}}{T_{amb}} . \rho_{CHE} . A_{CHE} . V_c . \Delta T & (22) \\ \Delta P_{tot} = \frac{\Delta T}{T_{amb}} g . \rho_{COL} . H_{CHE} & (23) \end{cases}$$

$$\begin{cases} \Delta P_s = \Delta P_{tot} - \frac{1}{2} \rho_C . V^2_c & (24) \\ V_c = \sqrt{2 . g H_{chem} . \frac{\Delta T}{T_{amb}}} & (25) \end{cases}$$

Where: chimney efficiency; total power carried by the flow; pressure difference between the chimney base and ambient conditions; and air velocity at the chimney inlet. η_{CHE} P_{TOT} ΔP_{tot} V_c

3. RESULTS AND DISCUSSION

3.1. Analysis of Mahajanga meteorological conditions

3.1.1. Meteorological characteristics of Mahajanga

Table 1: Geographic coordinates of the Mahajanga site

Latitude	Longitude	Altitude	LST reference meridian	Ground albedo	DEL
15.40’ Sud	46,21° Est	22 m	40°	0.35	0.9 h

Figure 4 shows changes in mean sunshine duration and mean wind speed in Mahajanga over 2010–2024. Monthly sunshine duration ranges from 169.39 h in January to 324.65 h in October, with a mean of 255.43 h per month, corresponding to an average of the monthly mean daily durations of 8.39 h.day-1. This pattern reflects seasonal sunshine variability, with January being the least sunny month and October the sunniest according to the data used. Mean wind speed reaches 3.72 m.s-1, with a minimum of 3.07 m.s-1 in March and a maximum of 4.37 m.s-1 in October. These parameters are important inputs for assessing solar gains and convective heat exchange at the collector.

International Journal of Progressive Sciences and Technologies (IJPSAT)
ISSN: 2509-0119.
© 2026 Scholar AI LLC.
https://ijpsat.org/
Vol. 60 No. 1 November 2026, pp. 496-517

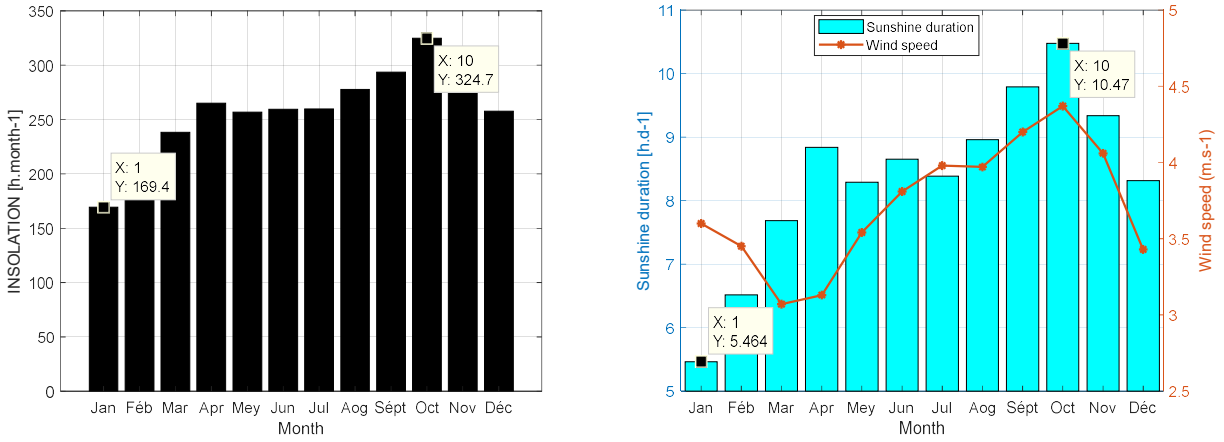

Figure 4: Variation in monthly mean sunshine duration and wind speed in Mahajanga

Figure 5 shows hourly variations in ambient and radiative sky temperatures, calculated from monthly mean minimum and maximum temperatures in Mahajanga for 2010–2024. For all twelve months, ambient temperature profiles increase gradually during the morning, reach a maximum around 12:48 in true solar time, and then decrease in the afternoon. Calculated ambient temperatures range approximately from 24.16 to 34.04 °C over the time interval studied.

Radiative sky temperature ranges approximately from 9.76 to 23.98 °C and remains below ambient temperature. In October, the corresponding maxima are 33.88 °C for ambient air and 23.75 °C for the sky, a difference of approximately 10.13 °C.

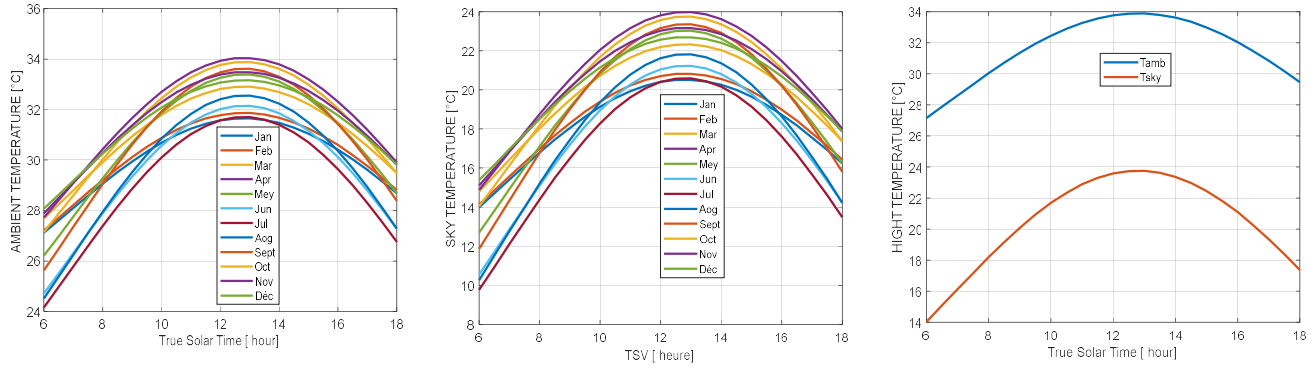

Figure 5: Temporal variation of ambient and sky temperatures

3.1.2. Evaluation of solar irradiance

Figure 6 shows the hourly variation of solar irradiance for three tilt angles (0°, −6°, and −15.40°) in October, the most favorable month in Mahajanga. The calculated maximum irradiances are 945.8, 949.7, and 941.2 W·m^{-2}, respectively. The −6° tilt yields the highest peak, 3.9 W·m^{-2} above the horizontal surface. These results show that the effect of tilt on maximum irradiance is limited and justify selecting −6° as the reference inclination for the subsequent thermal simulations.

International Journal of Progressive Sciences and Technologies (IJPSAT)
ISSN: 2509-0119.
© 2026 Scholar AI LLC.
https://ijpsat.org/
Vol. 60 No. 1 November 2026, pp. 496-517

Figure 7 shows hourly solar irradiance profiles for all twelve months of the year, at a −6° tilt, highlighting the favorable and unfavorable months. Irradiance increases in the morning, reaches a maximum near solar noon, and then decreases during the afternoon. Maximum values range from approximately 655.6 W·m⁻² in January to 949.7 W·m⁻² in October. This variation highlights the seasonal nature of Mahajanga's solar resource and justifies the use of January and October to analyze contrasting thermal conditions for the solar chimney power plant.

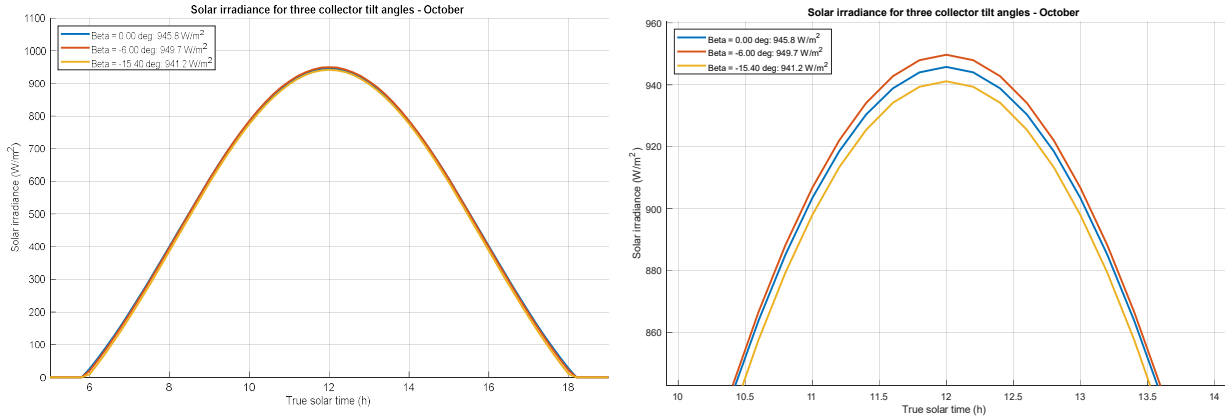

Figure 6: Effect of tilt angle on hourly solar irradiance in October at Mahajanga (2010–2024)

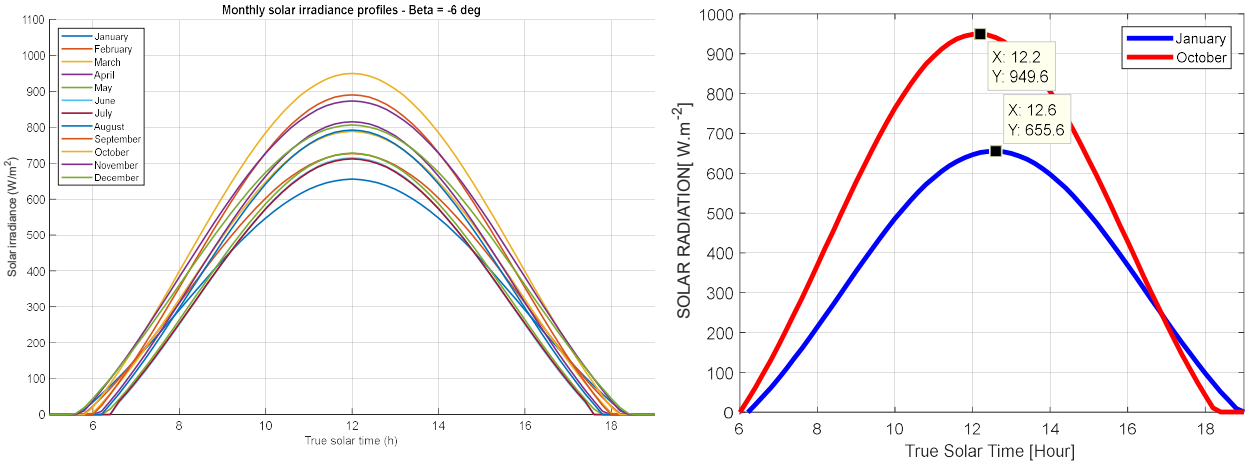

Figure 7: Hourly solar irradiance profiles for the twelve months in Mahajanga and for the favorable and unfavorable months

3.2. Quasi-steady-state thermal performance of the solar chimney power plant

3.2.1. Thermal performance of the Manzanares prototype under Mahajanga site conditions

The temperatures of the different collector components are shown in Figure 8: the transparent glazing, flowing fluid, cover, basin water, absorber, thermal-resistance layer, and ground, as functions of true solar time. They follow the temporal evolution of solar irradiance, forming a Gaussian-shaped curve (left panel). These temperatures increase as solar irradiance rises (right panel). They stop rising at solar noon and then gradually decline toward their morning values.

International Journal of Progressive Sciences and Technologies (IJPSAT)
ISSN: 2509-0119.
© 2026 Scholar AI LLC.
https://ijpsat.org/
Vol. 60 No. 1 November 2026, pp. 496-517

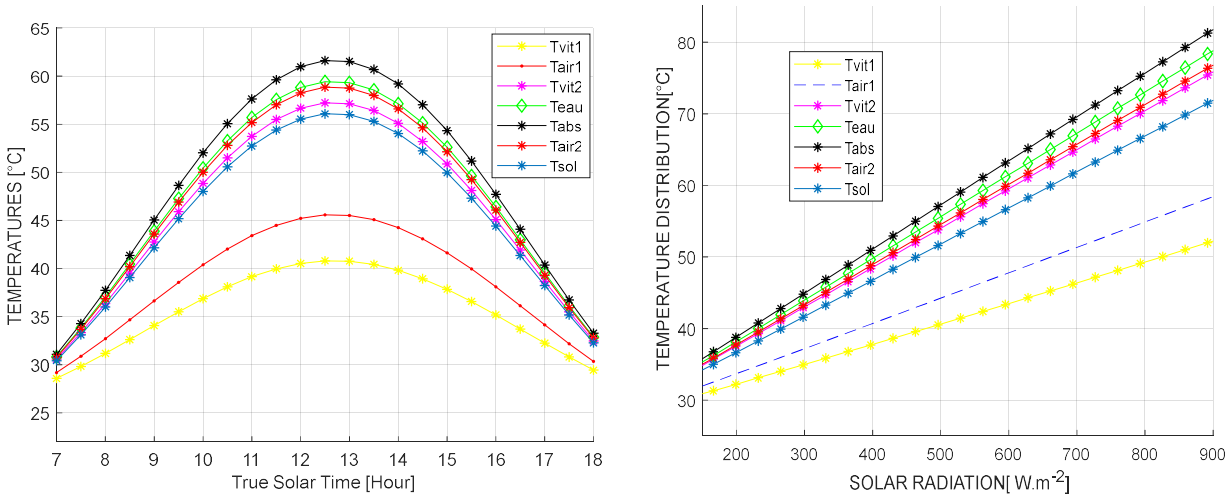

Figure 8: Temperature distribution within the collector and its dependence on solar irradiance

3.2.2. Comparison of configurations and selection of the reference geometry

Figure 9 compares the thermal performance of five solar chimney power plant configurations through water temperature, thermal power, and useful energy. Calculated maximum temperatures range from about 42 °C for Barison James to 77 °C for Mansoura. The Krisst configuration has a maximum temperature of approximately 67 °C.

Although its temperature is lower than that of Mansoura, Krisst is selected as the reference geometry because of its smaller dimensions, with a 6 m-diameter collector and a 10 m-high chimney. The clearance beneath its collector, estimated at 0.50 m, is also favorable for investigating the integration of a solar basin. This selection is based primarily on geometric suitability for the intended application rather than the highest temperature among the five cases. Krisst's thermal performance is then examined under Mahajanga meteorological conditions.

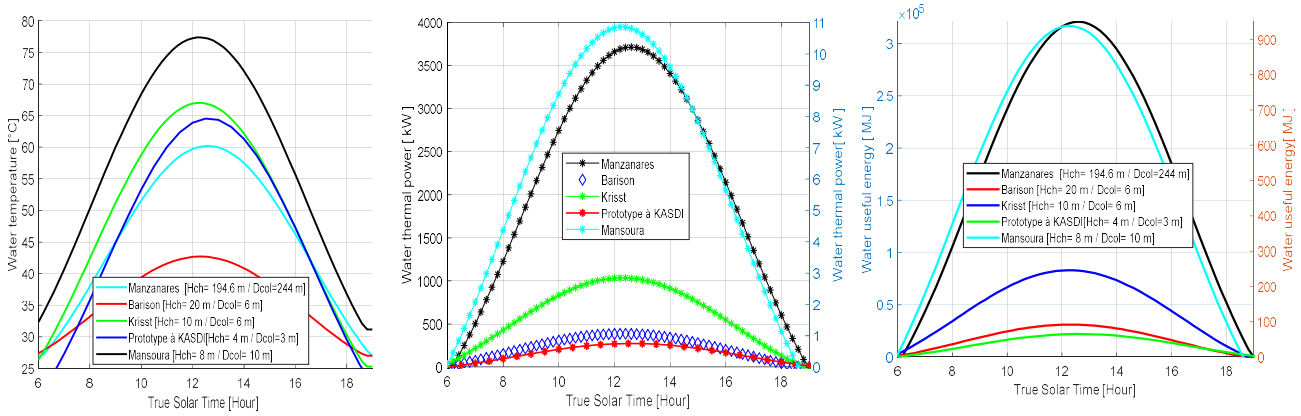

Figure 9: Temporal variation of water temperature, useful energy, and thermal power for the five proposed cases

International Journal of Progressive Sciences and Technologies (IJPSAT)
ISSN: 2509-0119.
© 2026 Scholar AI LLC.
https://ijpsat.org/
Vol. 60 No. 1 November 2026, pp. 496-517

3.2.3. Temperature distribution in the Krisst configuration

Figure 10 presents the hourly temperature distributions of the seven solar collector components for January and October in Mahajanga. The calculated profiles broadly follow the evolution of solar irradiance, with temperatures rising during the morning and reaching maxima around solar noon.

In January, at an irradiance of 655.43 W·m⁻², the absorber, water, and basin-cover temperatures reach 68.23, 67.19, and 66.15 °C, respectively. In October, at 949.37 W·m⁻², these values rise to 85.01, 83.51, and 82.00 °C. The absorber is thus the hottest component, followed by the water and basin cover. The upper glazing remains the coolest of the seven nodes, with maxima of 41.02 and 47.20 °C. Maximum water temperature increases by 16.31 °C from January to October, while maximum ambient temperature increases by only 2.23 °C. This difference highlights the strong effect of solar irradiance on the system's equilibrium temperatures.

However, water temperature remains below the atmospheric boiling point in both cases. These results indicate that the reference configuration, with the thermal parameters currently adopted, cannot establish the steam production required by the still. They justify further parametric analysis of the water-heating conditions.

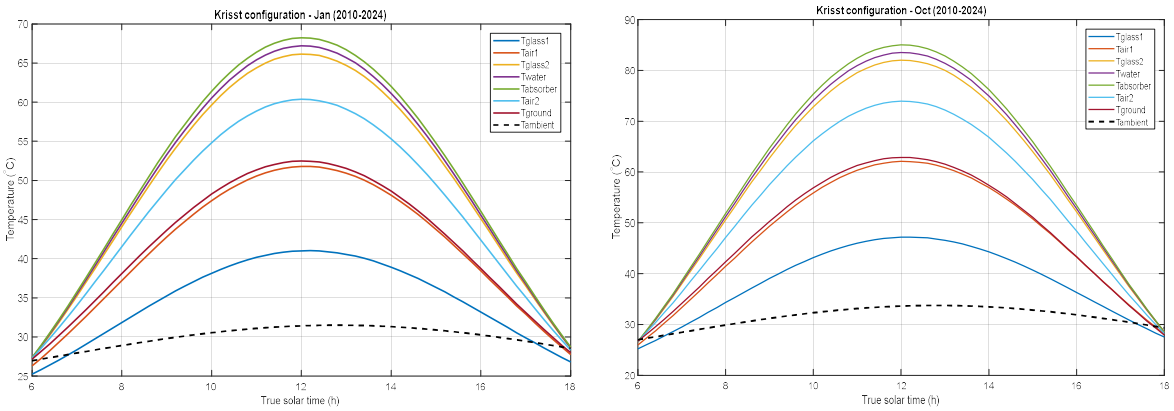

Figure 10: Temporal temperature distributions of the seven components of the solar chimney power plant

3.2.4. Parametric analysis of water temperature for the Krisst configuration

The parametric analysis aims to evaluate the influence of the main operating conditions on water temperature in the Krisst solar basin. Three parameters are examined: air mass flow rate, solar irradiance, and the optical and radiative properties of the two glazing covers.

The simulations vary each parameter in turn while keeping the others constant. This approach identifies factors that raise water temperature and assesses their influence on the system's thermal performance.

The results will be used to select operating conditions for subsequent investigation using the transient hybrid model, in order to evaluate heating time and theoretical vaporization potential.

3.2.4.1. Effect of air mass flow rate

Figure 11 shows the effect of air mass flow rate on water temperature in the Krisst configuration in January and October. Three values are examined: 0.01, 0.02, and 0.05 kg·s⁻¹. The results show that increasing mass flow rate decreases the maximum water temperature.

In January, the maximum falls from 88.36 °C to 73.02 °C when the flow rate increases from 0.01 to 0.05 kg·s⁻¹. In October, it decreases from 109.42 °C to 90.97 °C. Thus, 0.01 kg·s⁻¹ gives the highest equilibrium temperatures under both

International Journal of Progressive Sciences and Technologies (IJPSAT)
ISSN: 2509-0119.
© 2026 Scholar AI LLC.
https://ijpsat.org/
Vol. 60 No. 1 November 2026, pp. 496-517

climatic conditions. These findings show that air mass flow rate directly influences water thermal behavior in the model. However, 0.01 kg·s⁻¹ is only the most favorable water-heating condition among the three values examined.

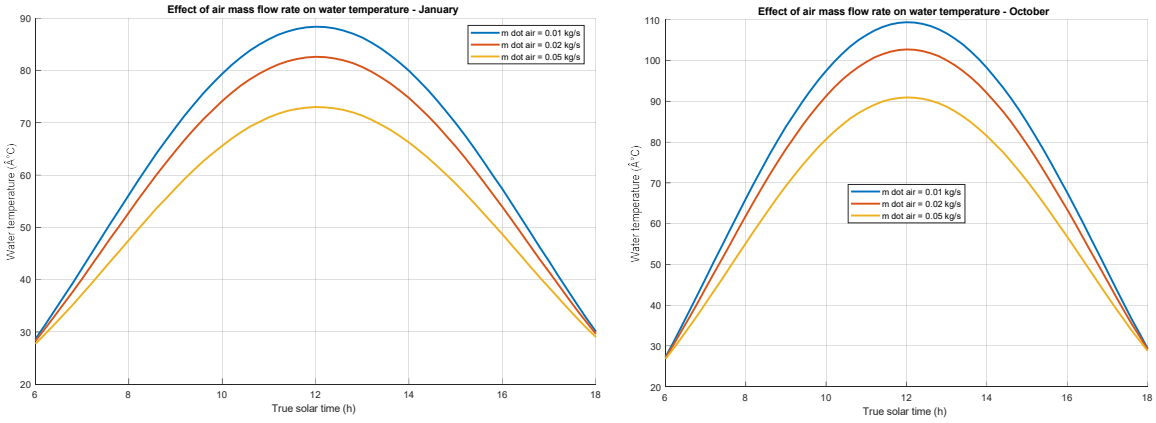

Figure 11: Effect of air mass flow rate on the hourly evolution of water temperature: January and October

3.2.4.2. Effect of seasonal variations in solar irradiance

Figure 12 compares the hourly evolution of water temperature in four representative months: January, April, July, and October. Calculated maximum temperatures are 88.36 °C, 101.65 °C, 90.82 °C, and 109.42 °C, respectively. October offers the most favorable conditions for water heating, whereas January produces the lowest maximum temperature. These results illustrate the influence of seasonal solar variations on the basin's thermal behavior. They also show that energy availability depends not only on peak irradiance but on all the meteorological conditions included in the model.

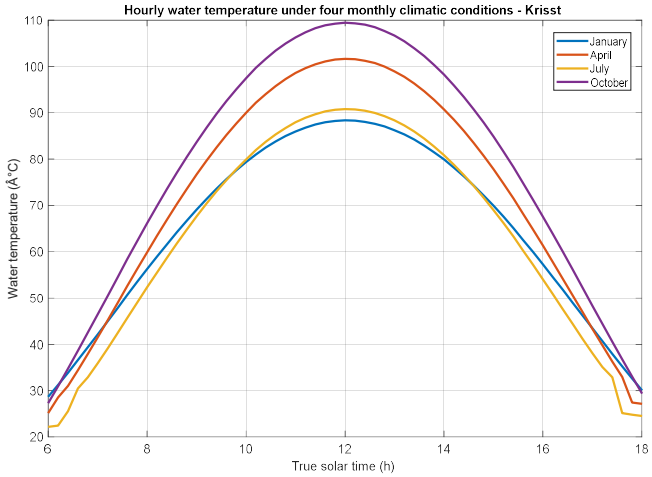

Figure 12: Effect of seasonal solar irradiance variations on the hourly evolution of water temperature

3.2.4.3. Effect of glazing-cover properties

Figure 13 compares hourly water temperatures for seven glazing-cover combinations in January and October. The results show that the glass–Low-E combination reaches the highest maximum temperatures, 99.31 °C in January and 130.36 °C in October. It is followed by quartz–Low-E, with corresponding values of 99.13 °C and 130.10 °C. Conversely, glass–P-film yields

International Journal of Progressive Sciences and Technologies (IJPSAT)
ISSN: 2509-0119.
© 2026 Scholar AI LLC.
https://ijpsat.org/
Vol. 60 No. 1 November 2026, pp. 496-517

the lowest temperatures. These results highlight the influence of the covers' optical and radiative properties on water heating. Glass–Low-E is therefore selected as the reference configuration for the remainder of the study.

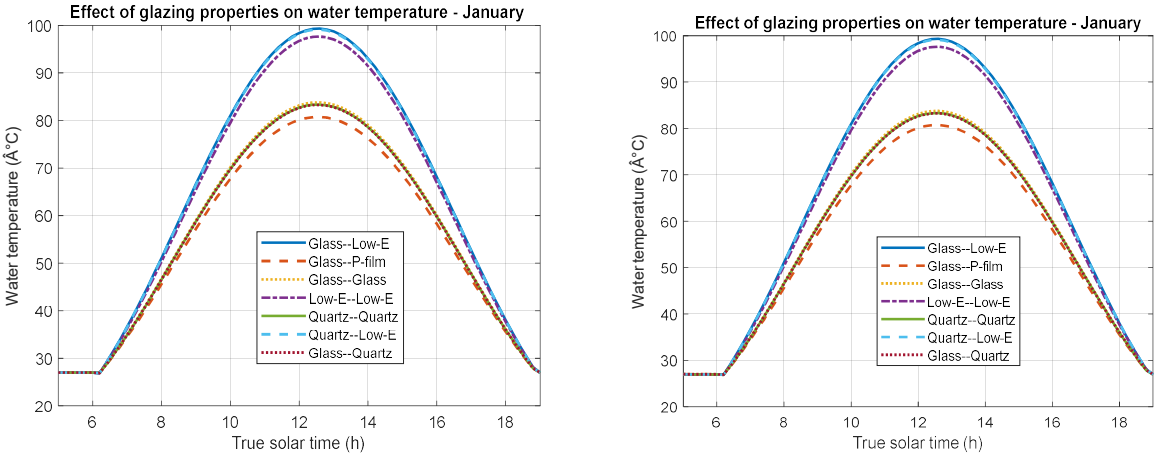

Figure 13: Effect of the physical properties of glazing covers on the hourly evolution of water temperature

The parametric analysis identified conditions favoring increased water temperature in the Krisst configuration. Among the flow rates tested, 0.01 kg·s^{-1} leads to the highest equilibrium temperatures. Glass–Low-E also performs best among the seven glazing combinations compared. In addition, monthly simulations show a significant effect of irradiance variability on water heating. These conditions are retained as references for further analysis. However, the quasi-steady-state model cannot represent heat accumulation in the water or determine the time required to reach boiling.

3.3. Transient thermal performance of the solar chimney power plant

3.3.1. Transient temperature distribution within the collector

Figure 14 shows the temporal evolution of temperatures at the seven thermal nodes of the Krisst configuration in January and October. The results show that temperatures do not immediately follow solar radiation changes. Indeed, they continue to rise after peak irradiance, reflecting the system's transient behavior.

This thermal lag is mainly explained by the thermal inertia of the components and gradual storage of absorbed energy. In particular, water has a high heat capacity, slowing its heating. Maximum temperatures are therefore observed after peak solar radiation, as expected for a system with thermal inertia.

Thermal response also varies by month. Maximum water temperature reaches 76.52 °C in January and 98.28 °C in October. This difference is associated with more favorable sunshine conditions in October. At an absolute pressure of 1 bar, water's saturation temperature is estimated at 99.61 °C. This value is not reached in either case. In October, however, maximum water temperature approaches this threshold, remaining 1.33 °C below it. Thus, under the reference conditions considered, the model does not yet predict steam production.

International Journal of Progressive Sciences and Technologies (IJPSAT)
ISSN: 2509-0119.
© 2026 Scholar AI LLC.
https://ijpsat.org/
Vol. 60 No. 1 November 2026, pp. 496-517

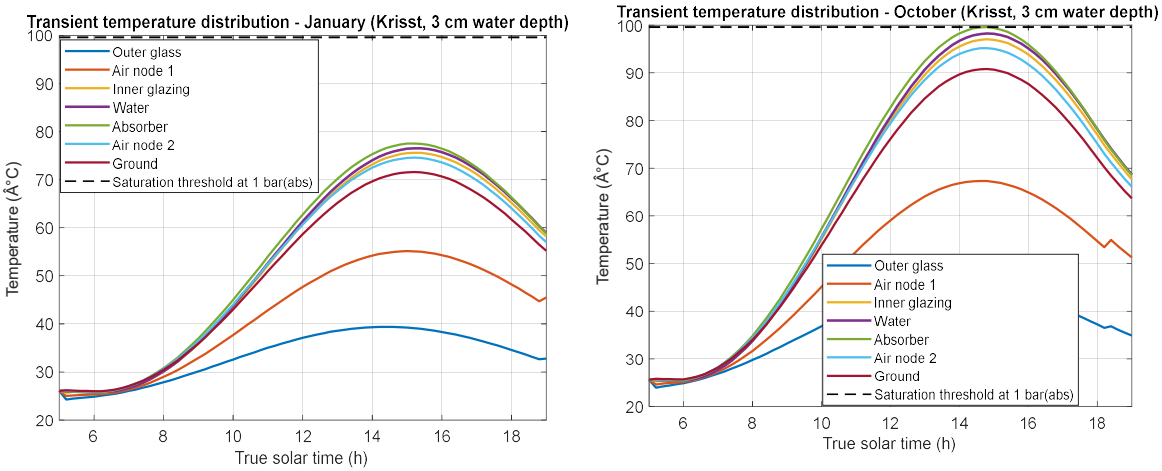

Figure 14: Temporal evolution of the temperatures of the seven thermal nodes under transient conditions

3.3.2. Comparison of quasi-steady-state and transient regimes

Figure 15 compares hourly water temperature and solar irradiance in October under quasi-steady-state and transient conditions. In the quasi-steady-state regime, water temperature closely follows irradiance changes and reaches a theoretical maximum of 129.34 °C at 12:12, corresponding to the solar maximum of 949.57 W/m². In contrast, the transient model predicts a maximum temperature of 98.28 °C at 14:48, a delay of 2 h 36 min.

This delay results mainly from the thermal inertia of water, which gradually accumulates incoming energy. Heating continues after peak irradiance as long as thermal inputs exceed losses. The transient regime therefore provides a more faithful representation of heating time and the system's thermal phase lag.

However, the quasi-steady-state temperature above 99.61 °C is a theoretical prediction of the model without phase change. It is not physically admissible for liquid water at an absolute pressure of 1 bar. This comparison thus highlights the need to include thermal inertia and, when studying vaporization, latent heat to assess steam production correctly.

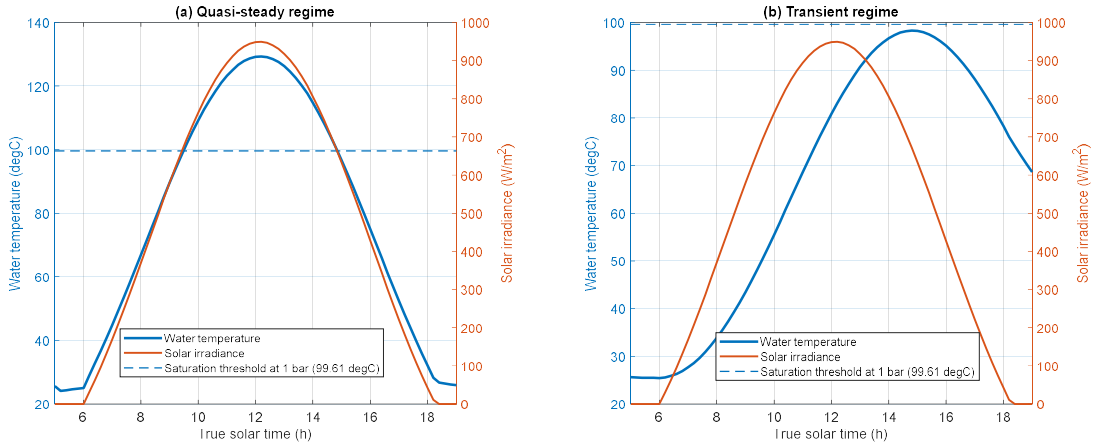

Figure 15: Comparison of hourly water temperature and solar irradiance in October under quasi-steady-state and transient conditions

International Journal of Progressive Sciences and Technologies (IJPSAT)
ISSN: 2509-0119.
© 2026 Scholar AI LLC.
https://ijpsat.org/
Vol. 60 No. 1 November 2026, pp. 496-517

3.3.3. Effect of water-layer thickness

Figures 16 and 17 present the evolution of water temperature and cumulative steam production, respectively, for water depths of 1, 2, and 3 cm in January and October at an absolute pressure of 1 bar. The results show that reducing water depth promotes faster heating, mainly by lowering water mass and thermal inertia.

In January, maximum temperatures are 93.48, 84.89, and 77.32 °C for water depths of 1, 2, and 3 cm, respectively. None reaches the saturation temperature of 99.61 °C. In contrast, more favorable October sunshine allows the 1 and 2 cm layers to reach saturation at 10:52 and 12:28 true solar time, respectively. The 3 cm layer remains below this threshold, with a maximum temperature of 98.87 °C.

Theoretical steam production reaches 31.57 kg for a 1 cm layer, compared with 16.17 kg for 2 cm. This difference is mainly due to saturation being reached earlier, allowing more time for incoming heat to be converted into latent heat. Thus, reducing the layer thickness from 2 to 1 cm increases the calculated cumulative steam mass by about 95%. These results identify the 1 cm layer as the most favorable among the configurations investigated.

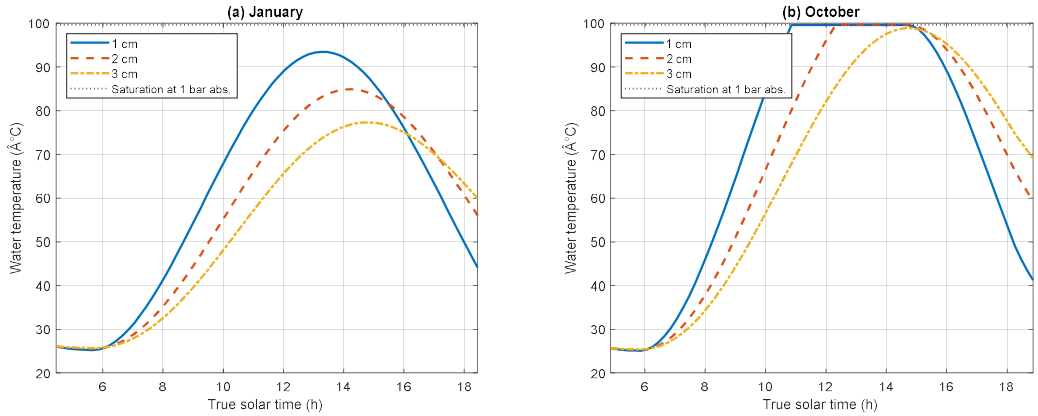

Figure 16: Effect of water-layer thickness on its transient temperature evolution: January and October

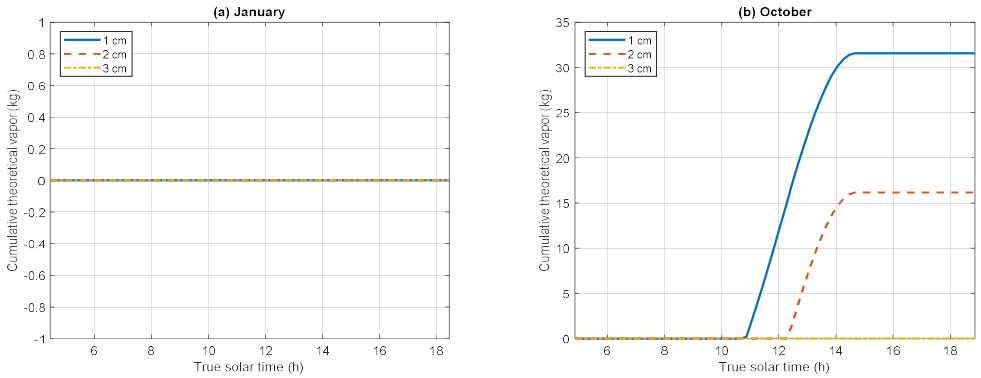

Figure 17: Effect of water-layer thickness on cumulative steam production: January and October

International Journal of Progressive Sciences and Technologies (IJPSAT)
ISSN: 2509-0119.
© 2026 Scholar AI LLC.
https://ijpsat.org/
Vol. 60 No. 1 November 2026, pp. 496-517

3.3.4. Summary of performance and potential steam supply to the still

Table 2: Comparison of thermal performance

Indicator in October	1 cm	2 cm	3 cm
Température maximale	99,61 °C	99,61 °C	98,87 °C
Début de saturation (TSV)	10 h 52	12 h 28	Not reached
Débit maximal de vapeur	11,10 kg/h	10,65 kg/h	0
Masse cumulée de vapeur	31,57 kg	16,17 kg	0

The results show that the 1 cm configuration can produce a cumulative steam mass of 31.57 kg in October, at a maximum flow rate of 11.10 kg/h. Vaporization begins around 10:52 true solar time and continues for approximately four hours, at a rate varying with available thermal input. However, production remains intermittent and sunshine-dependent. In January, none of the depths considered reaches saturation. The plant's capacity to supply a still therefore cannot be guaranteed throughout the year.

3.4. Experimental results of essential oil extraction using the FSTE Mahajanga unit

3.4.1. Analysis of the results obtained

The experimental results come from six distillations carried out at the Essential Oil Extraction Unit of FSTE, University of Mahajanga. The trials involved three aromatic plants: Niaouli (Melaleuca quinquenervia), Kininina (Eucalyptus sp.), and Ravintsara (Cinnamomum camphora). Extraction was performed by indirect steam distillation using a wood-fired boiler.

The plants investigated are listed in Table 2, with details of collection site, distillation date, quantity of plant material, and vernacular name. Several extractions were carried out using different quantities. Three Eucalyptus distillations were performed at different times, as well as two distillations of Melaleuca quinquenervia. For Cinnamomum camphora, leaves were brought by collectors from Fandriana (Amoron'i Mania). Only one distillation was carried out because this plant is rare in our region and available in small quantities.

Table 3: Plants collected for extraction

Plant name	**Collection site**	**Distillation date**	**Plant material quantity**
Melaleuca quinquinervia (Niaouli or Kininin-drano)	Belobaka, Mahajanga II	07/06/2021	68 kg
	Belobaka, Mahajanga II	19/11/2021	96 kg
Eucalyptus sp (Kininina)	Ambondrona, Mahajanga I	18/12/2021	156, 5 kg
	Ambondrona, Mahajanga I	04/11/2021	62 kg
	BESELY, Belobaka	31/05/2021	80 kg
Cinnamomum camphora (ravintsara)	Fandriana, Amoron'i mania	14/01/2022	16 kg

Table 4 presents the experimental results for three plant types collected in different quantities and distilled separately. Only leaves were used. Distillation was performed manually, using dry wood as fuel and tap water as the steam source.

International Journal of Progressive Sciences and Technologies (IJPSAT)
ISSN: 2509-0119.
© 2026 Scholar AI LLC.
https://ijpsat.org/
Vol. 60 No. 1 November 2026, pp. 496-517

Table 3: Experimental results

Plant name	Quantity	Heating time	Extraction time	V_{HE}	R_{HE}	Floral water volume
Melaleuca quinquinervia	68 Kg	49min	2 h 21min	150 mL	0,22 %	16,5 L
	96 Kg	50 min	2 h 20 min	150 mL	0,17 %	7,7 L
Eucalyptus sp	156,5 Kg	38 min	2h 16 min	650 mL	0,42 %	20 L
	62 Kg	85 min	3 h 15 min	405 mL	0,65 %	3,5 L
	80 Kg	60 min	2h 20 min	110 mL	0,13 %	20 L
Cinnamomum camphora	16 Kg	62min	1h 54 min	160 mL	1 %	7 L

The yields obtained vary according to plant species and distillation conditions. For Niaouli, they reach 0.22% and 0.17%, with the same essential oil volume of 150 mL. Kininina shows greater variability, with yields between 0.13% and 0.65%. The maximum yield of 0.65% is obtained after an extraction time of 3 h 15 min. For Ravintsara, extracting 16 kg of leaves produces 160 mL of essential oil, corresponding to a yield of 1%, after 1 h 54 min of extraction.

These variations indicate that the quantity of plant material alone does not determine extraction yield. Treatment time, leaf characteristics, and operating conditions may also play a role. The experimental results thus provide a reference for examining the potential use of steam generated by the solar chimney power plant.

3.4.2. Comparison of experimental results with previous studies

Table 4 compares the experimental yields of the three aromatic plants with values reported in previous studies. The results show varying discrepancies depending on the plant species and extraction conditions.

For Kininina, experimental yields range from 0.13 to 0.65%, compared with 1.20% in the reference study. The highest yield is obtained after 3 h 15 min of extraction, suggesting an effect of treatment duration. Niaouli has lower yields of 0.17 and 0.22%, compared with 2% in the literature. Ravintsara's 1% yield is closer to the reference value of 1.80%, despite an extraction time limited to 1 h 54 min.

These differences may be related to distillation duration, plant material characteristics, and steam-production conditions. However, because the trials used different quantities of leaves and lacked precise steam temperature and flow measurements, these discrepancies cannot be attributed to any single factor.

These results highlight the value of better control over distillation thermal conditions. They provide an experimental basis for investigating the potential coupling of the solar chimney power plant and still, without yet allowing direct prediction of yields obtained using solar steam.

Table 4: Comparison of experimental results (FSTE still) with previous studies

Plant name	Experimental result			Previous studies [25], [26], [27]			
	Temps d'extract.	V_{HE}	Yield	Extraction time	Steam T°	V_{HE}	Yield
Kininina	2,27 h	650 mL	0,42 %	3 à 5h	120 à 140 °C	1878 mL	1,2 %
	3,25 h	405 mL	0,65 %				
	2,33 h	110 mL	0,13 %				
Niaouli	2,35 h	150 mL	0,22 %	2 à 4h	100 à 120 °C	1363 mL	2 %
	2,33 h	150 mL	0,17 %				
Ravintsara	1,9 h	160 mL	1 %	1 à 3h	100 à 150 °C	288 mL	1,8 %

3.5. **Assessment of the coupling between the solar chimney power plant and the still**

The coupling assessment compares the solar steam simulated for January and October with mean condensate flow rates estimated from experimentally recovered floral-water volumes. For the six distillations performed at FSTE Mahajanga, these flow rates range from 1.08 to 8.82 kg/h depending on the plant and extraction conditions.

Table 5: Flow-rate estimates from experimental results

Plant and trial	Floral water (L)	Duration (h)	Mean flow rate (kg/h)
Niaouli — 68 kg	16,5	2,35	**7,02**
Niaouli — 96 kg	7,7	2,33	**3,30**
Kininina — 156,5 kg	20	2,27	**8,82**
Kininina — 62 kg	3,5	3,25	**1,08**
Kininina — 80 kg	20	2,33	**8,57**
Ravintsara — 16 kg	7	1,90	**3,68**

The most demanding case in terms of recovered condensate is Kininina (156.5 kg), at 8.82 kg.h-1. This represents approximately 79.5% of the maximum simulated solar steam flow rate in October. In January, despite a maximum water temperature of 93.48 °C for a 1 cm depth, saturation is not reached. Therefore, the model predicts no steam production by boiling. In October, by contrast, saturation is reached at 10:52 true solar time. Maximum steam flow rate reaches 11.10 kg/h, with cumulative production of 31.57 kg.

Table 6: Comparison with solar steam in January and October

Parameter	**January**	**October**
Épaisseur retenue	1 cm	1 cm
Maximum water temperature	93,48 °C	99,61 °C
Saturation atteinte	No	Yes, at 10:52 true solar time
Débit maximal de vapeur	**0 kg/h**	**11,10 kg/h**
Masse cumulée de vapeur	**0 kg**	**31,57 kg**

International Journal of Progressive Sciences and Technologies (IJPSAT)
ISSN: 2509-0119.
© 2026 Scholar AI LLC.
https://ijpsat.org/
Vol. 60 No. 1 November 2026, pp. 496-517

This maximum flow rate is higher than the mean condensate flow rates measured experimentally. The results indicate promising energy potential in October, unlike January, when steam production is insufficient.

Nevertheless, the flow rates calculated from floral-water volumes do not necessarily represent all the steam consumed. Furthermore, the availability of 31.57 kg of steam over the simulated period does not guarantee a sufficient flow rate throughout the extraction period. Steam transport to the still also depends on thermal losses, pressure losses, and available driving pressure.

Thus, the coupling shows favorable potential in October, but its operational feasibility remains to be confirmed by comparing hourly steam production and demand profiles, and verifying transport conditions to the extraction vessel.

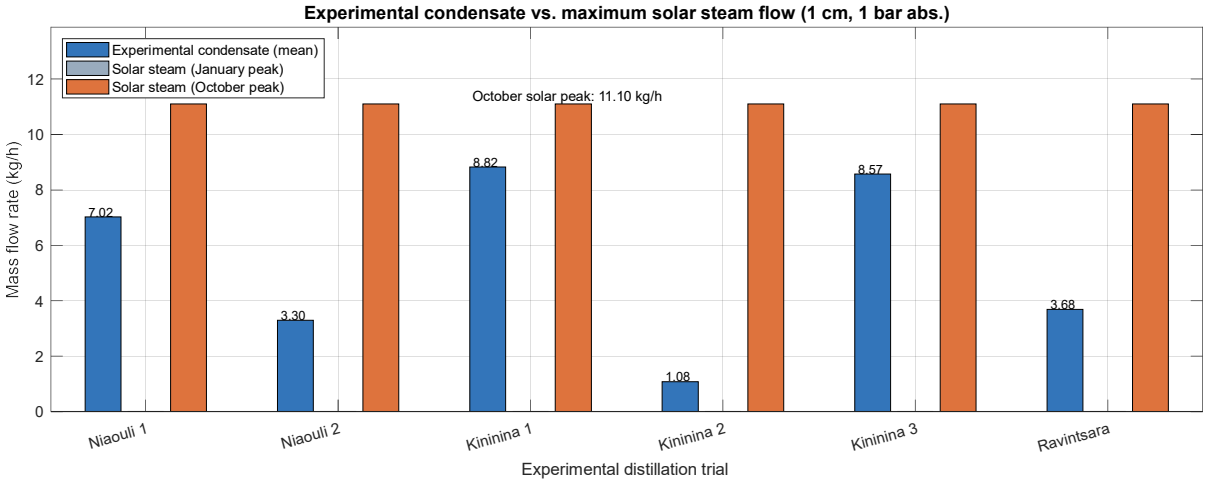

Figure 18: Mean recovered condensate flow rates in six trials and maximum simulated solar steam flow rates in October and January

4. CONCLUSION

This study evaluated the thermal potential of a solar chimney power plant intended to generate steam for essential oil extraction. Analysis of meteorological data for Mahajanga over 2010–2024 revealed seasonal sunshine variability, with maximum irradiances of 655.57 W.m-2 in January and 949.57 W.m-2 in October. The seven-node thermal model and parametric analysis examined the effects of irradiance, air mass flow rate, glazing properties, and water-layer thickness on system performance. The Glass–Low-E combination promotes water heating, while comparison of quasi-steady-state and transient regimes reveals a thermal delay of 2 h 36 min in October, mainly due to water inertia. Among 1, 2, and 3 cm depths, the 1 cm layer gives the best performance. At 1 bar absolute pressure, it reaches saturation at 10:52 in October, with a cumulative theoretical steam production of 31.57 kg and a maximum flow rate of 11.10 kg.h-1. In contrast, no steam generation by boiling is predicted in January. Experimental trials performed at FSTE Mahajanga using Niaouli, Kininina, and Ravintsara gave essential oil yields between 0.13 and 1%. Estimated mean recovered condensate flow rates, between 1.08 and 8.82 kg.h-1, remain below the maximum calculated solar steam flow rate in October. This comparison highlights coupling potential during the favorable month without guaranteeing a continuous supply to the still. Operational feasibility still requires assessment of thermal losses, pressure drops, and actual steam availability in the extraction vessel. Looking ahead, an auxiliary electric heating device is necessary to offset insufficient power during periods of low solar irradiance and stabilize steam production. This improvement would help ensure a more regular supply to the still and enhance the reliability of the essential oil extraction system.

REFERENCES:

[1] BOUKHATEM Mohamed Nadjib, FERHAT Amine and KAMELI Abdelkrim, Methods for the extraction and distillation of essential oils: literature review, 2019

[2] Christophe Alleau, BTS CIR Lecturer, Fuel-fired steam boilers, 2011 edition

[3] NAÏT SIDI AHMED Amina, ALLOUACHE Louisa, Potential for integrating renewable energies into a mobile essential oil extraction unit, 2009

[4] Soukaina HILALI, Thermal solar energy applications on ecoextraction and drying of orange peels and rosemary leaves, 2020

[5] Waldan GIRARD and Rohan NOWAK, How to distill floral waters using solar energy? A solidarity-based, sustainable and societal project, 2016

[6] Hakim SEMAI & Amor BOUHDJAR, Modeling a solar chimney power plant under turbulent conditions with thermal storage.

[7] Mr S. BEKKOUCHE. Modeling the Thermal Behavior of Selected Solar Devices. Electronics and Modeling specialization. Doctoral dissertation, Abou-Bakr Belkaid University, Tlemcen (2008).

[8] Afef JANNEN, Hatem MHIRI, Philippe BOURNOT, Numerical analysis of aerothermal behavior in a solar chimney.

[9] Schlaich, J., Bergermann, R., Schiel, W., & Weinrebe, G. (2005). Design of Commercial Solar Updraft Tower Systems—Utilization of Solar Induced Convective Flows for Power Generation. Journal of Solar Energy Engineering, 127(1), 117–124.

[10] Bernardes, M. A. dos S., Voß, A., & Weinrebe, G. (2003). Thermal and technical analyses of solar chimneys. Solar Energy, 75(6), 511–524. DOI : 10.1016/j.solener.2003.09.012.

[11] Kreetz H., Theoretical investigations and design of a temporary water storage system for the solar updraft tower. Diploma, Energy Process Engineering and Renewable Energy Conversion Technologies EVUR, Technical University of Berlin.

[12] M. SEMAI Hakim, Investigation of an optimal configuration of a solar chimney power plant, 2017.

[13] ACHOURI El Hadj, Contribution to the experimental study of a solar chimney in Algeria, doctoral dissertation, Kasdi Merbah University Ouargla, 2021

[14] R. BARISON James, Electricity generation by a solar chimney, dissertation, University of Antananarivo, 2012.

[15] Krisst R.J.K, Energy transfer systems. Alternat source energy, vol 63, 1983

[16] M.S. Anter, Ahmed Ramzy and Ahmed M. Hamed, Case Study of a Solar Chimney in Mansoura, Egypt ;

[17] Martínez-Lozano, J. A., Tena, F., Onrubia, J. E., & de la Rubia, J. (1984). The historical evolution of the Ångström formula and its modifications: Review and bibliography. Agricultural and Forest Meteorology, 33(2–3), 109–128.

[18] Von Allwörden, H., Gasser, I., & Kamboh, M. (2018). Modelling, simulation and optimisation of general solar updraft towers. Applied Mathematical Modelling, 64, 265–284

[19] DONA Victorien Bruno, MAXWELL Djaffard, RATIARISON Adolphe Andriamanga, Evaluation of solar energy resources in Mahajanga: Solar irradiation on a horizontal surface, 2019

[20] Bergman, T. L., Lavine, A. S., Incropera, F. P., & DeWitt, D. P. Fundamentals of Heat and Mass Transfer.

[21] Khalilian, M. (2017). Experimental investigation and theoretical modelling of heat transfer in circular solar ponds by lumped capacitance model. Applied Thermal Engineering, 121, 737–749.

[22] Gortych, M., Lipnicki, Z., Małolepszy, T., & Grabas, P. (2024). Solar Chimney Operation Variant. Energies, 17(19), 5004.

[23] Hollands, K. G. T., Raithby, G. D., & Konicek, L. (1975). International Journal of Heat and Mass Transfer, 18(7–8), 879–884.

[24] Dai YJ, Huang HB, Wang NRZ. Case study of solar chimney power plants in North-western regions of China. Renewable Energy 2003 ; 28 : 1295-304.

[25] Faramalala R., Effect of leaf and plant age on essential oil yield and quality in ravintsara (Cinnamomum camphora), postgraduate research dissertation in Plant Biology and Ecology, Plant Physiology specialization, University of Antananarivo, Faculty of Sciences, Department of Plant Biology and Ecology, 2009

[26] Amira Radia ZERHOUNI, Modeling mass transfer during essential oil and polyphenol extraction from Laurus nobilis L. by hydrodistillation, Master's dissertation in Chemical Engineering, 2017

[27] Schlaich, J., Bergermann, R., Schiel, W., & Weinrebe, G. (2005). Design of Commercial Solar Updraft Tower Systems—Utilization of Solar Induced Convective Flows for Power Generation. Journal of Solar Energy Engineering, 127(1), 117–124.